



One-step fabrication of $g\text{-C}_3\text{N}_4$ nanosheets/ TiO_2 hollow microspheres heterojunctions with atomic level hybridization and their application in the multi-component synergistic photocatalytic systems



Kai Wei, Kexin Li*, Liushui Yan, Shenglian Luo*, Huiqin Guo, Yuhua Dai, Xubiao Luo

Key Laboratory of Jiangxi Province for Persistent Pollutants Control and Resources Recycle, NanChang Hangkong University, NanChang 330063, People's Republic of China

ARTICLE INFO

Keywords:
Synergistic photocatalytic effects
Nanosheets
Hollow microspheres
Heterojunctions
Composite pollution systems

ABSTRACT

In this paper, graphitic carbon nitride nanosheets/titanium dioxide hollow microspheres heterojunctions ($g\text{-C}_3\text{N}_4$ NSS/ TiO_2 HMSs) with excellent photocatalytic activity were successfully fabricated by a simple one-step synthesis strategy in the assistance of hydrothermal carbon microspheres. Hydrothermal carbon microspheres act as both dispersant and structure-directing agent for the simultaneous construction of graphitic carbon nitride nanosheets and titanium dioxide hollow microspheres. The synergistic photocatalytic effects in the 4-fluorophenol/hexavalent chromium [4-FP/Cr(VI)] and hexavalent chromium/trivalent arsenic [Cr(VI)/As(III)] multi-component composite pollution systems were studied by using as-prepared $g\text{-C}_3\text{N}_4$ NSS/ TiO_2 HMSs under different pH conditions. Interestingly, the efficiencies of 4-FP degradation, Cr(VI) reduction, and As(III) oxidation were simultaneously improved in the 4-FP/Cr(VI) and Cr(VI)/As(III) multi-component synergistic photocatalytic systems relative to the single-component photocatalytic systems. The synergistic photocatalytic mechanisms in the 4-FP/Cr(VI) and Cr(VI)/As(III) multi-component synergistic photocatalytic systems were systematically discussed.

1. Introduction

In brief, the synergistic effects are “ $1 + 1 > 2$ ” effects. In chemistry, the synergistic effects mean that the effects produced by the combination of two or more components are greater than the sum of the effects produced by the individual components alone [1–4]. In the field of photocatalysis, the synergistic effects objectively exist in both photocatalysts and photocatalytic reactions. However, most of the researchers focus on the synergistic effects in the photocatalysts, while the synergistic effects in the photocatalytic reactions have seldom been studied [5–8].

In the preparation of photocatalysts, the construction of composite semiconductor heterojunctions is based on the synergistic effects between semiconductor components [9–13]. Specifically, the recombination of photogenerated carriers is effectively inhibited due to the transfer of photogenerated carriers between the interfaces of the semiconductor components. Therefore, the photocatalytic activity of composite semiconductor heterojunctions is higher than that of each pure semiconductor in the components. Over the past decade, graphitic carbon nitride ($g\text{-C}_3\text{N}_4$) and titanium dioxide (TiO_2) semiconductor photocatalysts have been widely applied in the field of environmental

photocatalysis because of their own advantages, such as low cost, environmentally friendly, and high stability [14–19]. Therefore, the construction of $g\text{-C}_3\text{N}_4$ / TiO_2 heterojunctions has always been a hot issue in the development of new photocatalytic materials [20–22]. However, there are two bottlenecks in the current construction technique of $g\text{-C}_3\text{N}_4$ / TiO_2 heterojunctions. On the one hand, the preparation of $g\text{-C}_3\text{N}_4$ and TiO_2 components is usually separate in the course of $g\text{-C}_3\text{N}_4$ / TiO_2 heterojunctions construction due to the different preparation methods of $g\text{-C}_3\text{N}_4$ and TiO_2 . Therefore, the hybridization of $g\text{-C}_3\text{N}_4$ and TiO_2 components at the atomic level can't be achieved. On the other hand, it is also difficult to simultaneously control the morphology of $g\text{-C}_3\text{N}_4$ and TiO_2 components through the one-step synthesis strategy in the course of $g\text{-C}_3\text{N}_4$ / TiO_2 heterojunctions construction due to the different chemical properties of precursors for the $g\text{-C}_3\text{N}_4$ and TiO_2 preparation. For example, ordered mesoporous TiO_2 can be easily produced by the surfactant template strategy in the organic solvent [23–25]. However, the self-assembly process between $g\text{-C}_3\text{N}_4$ precursor and surfactant can't be accomplished in the organic solvent. In addition, Yang et al. successfully fabricated $g\text{-C}_3\text{N}_4$ nanosheets by a liquid-exfoliation method from bulk $g\text{-C}_3\text{N}_4$ powders [26]. Obviously, this method isn't suitable for the morphology controllable synthesis of TiO_2 .

* Corresponding authors.

E-mail addresses: lihx880@hotmail.com (K. Li), sllou@hnu.edu.cn (S. Luo).

Multi-component composite pollution systems are widely distributed in nature with the rapid development of industry and agriculture, such as electroplating wastewater, sludge in the polluted water treatment plant, and garbage of urban life [27–29]. In recent decades, photocatalytic technology has been widely used to solve environmental pollution problems since the photocatalytic hydrogen production from water-splitting was discovered in 1972 [30–33]. For example, aqueous organic pollutants can be degraded to carbon dioxide and water by photocatalytic oxidation process, photogenerated electrons can reduce the highly toxic hexavalent chromium [Cr(VI)] in aqueous dichromate ($\text{Cr}_2\text{O}_7^{2-}$) to low toxic trivalent chromium [Cr(III)], highly toxic trivalent arsenic [As(III)] can be oxidized to low toxic pentavalent arsenic [As(V)] through photocatalytic oxidation process [34–39]. However, in the current environmental photocatalysis field, most of the researchers focus on the development of novel photocatalysts and testing the photocatalytic activity of the developed materials in a single-component photocatalytic system but ignore the synergistic effects contained in the photocatalytic reactions [40–43]. In fact, through the synergistic effects in the photocatalytic reactions to solve the composite pollution problems have very great practical significance. But unfortunately, the synergistic photocatalytic effects and mechanisms in the multi-component composite pollution systems haven't been studied systematically so far.

In this paper, $\text{g-C}_3\text{N}_4$ nanosheets/ TiO_2 hollow microspheres heterojunctions ($\text{g-C}_3\text{N}_4$ NSs/ TiO_2 HMSs) with excellent photocatalytic activity were successfully fabricated by a simple one-step synthesis strategy in the assistance of hydrothermal carbon microspheres. Hydrothermal carbon microspheres prepared directly from waste *Camellia oleifera* shells act as both dispersant for the construction of $\text{g-C}_3\text{N}_4$ nanosheets and structure-directing agent for the construction of TiO_2 hollow microspheres during the preparation of $\text{g-C}_3\text{N}_4$ NSs/ TiO_2 HMSs. The atomic level hybridization was successfully achieved between the semiconductor components in the $\text{g-C}_3\text{N}_4$ NSs/ TiO_2 HMSs due to the one-step introduction of melamine and titanium butoxide precursors. We preliminarily studied the photocatalytic activity of as-prepared $\text{g-C}_3\text{N}_4$ NSs/ TiO_2 HMSs under different pH conditions in the single-component photocatalytic systems, such as 4-fluorophenol (4-FP) degradation, Cr(VI) reduction, and As(III) oxidation. Subsequently, we further studied the synergistic photocatalytic effects in the 4-FP/Cr(VI) and Cr(VI)/As(III) multi-component composite pollution systems by using as-prepared $\text{g-C}_3\text{N}_4$ NSs/ TiO_2 HMSs under different pH conditions. As a result, compare with single-component photocatalytic systems, it was found that the degradation efficiency of 4-FP, the reduction efficiency of Cr(VI), and the oxidation efficiency of As(III) were simultaneously improved in the 4-FP/Cr(VI) and Cr(VI)/As(III) multi-component synergistic photocatalytic systems. At last, we systematically discussed the synergistic photocatalytic mechanisms in the 4-FP/Cr(VI) and Cr(VI)/As(III) multi-component synergistic photocatalytic systems.

2. Experimental

2.1. Chemicals and reagents

Hydrothermal carbon microspheres (HCMSs) were obtained directly from waste *Camellia oleifera* shells according to our previous work [44,45]. Melamine ($\text{C}_3\text{H}_6\text{N}_6$, AR grade) was purchased from Tianjin Damao Chemical Reagent. Titanium butoxide ($\text{Ti}(\text{OC}_4\text{H}_9)_4$, $\geq 99.0\%$, abbreviated TBT), 4-fluorophenol ($\text{C}_6\text{H}_5\text{OF}$, 99%, abbreviated 4-FP), and potassium dichromate ($\text{K}_2\text{Cr}_2\text{O}_7$, AR grade) were purchased from Aladdin Chemistry Co. Ltd. Sodium arsenite (NaAsO_2 , AR grade) and disodium hydrogen arsenate ($\text{Na}_2\text{HAsO}_4 \cdot 7\text{H}_2\text{O}$, AR grade) were purchased from Chengdu Echo Chemical Reagent.

2.2. Preparation of $\text{g-C}_3\text{N}_4$ NSs/ TiO_2 HMSs by a simple one-step synthesis strategy in the assistance of HCMSs

In a typical synthesis, 0.75 g HCMSs and 1.5 g melamine were uniformly dispersed into 100 mL EtOH using a 500 W ultrasonic cracher for 15 min, and then 0.3 mL $\text{NH}_3\text{H}_2\text{O}$ was added. After vigorous stirring for 30 min, 0.75 mL TBT were successively added drop wise, and then stir the obtained HCMSs/melamine/TBT/EtOH/ $\text{NH}_3\text{H}_2\text{O}$ suspension at 45 °C for 24 h. After centrifugation, the resulting solid product was washed three times with H_2O and EtOH respectively, and then dried at 60 and 100 °C for 12 h respectively. After calcining at 500 °C for 2 h, the final product was obtained and denoted as $\text{g-C}_3\text{N}_4$ NSs/ TiO_2 HMSs. For comparison, bulk $\text{g-C}_3\text{N}_4$ was prepared by directly calcining melamine at 500 °C for 2 h. TiO_2 , TiO_2 HMSs, and $\text{g-C}_3\text{N}_4/\text{TiO}_2$ were prepared by the same method as above but in the absence of HCMSs/melamine, melamine, and HCMSs.

2.3. Characterizations

Field emission scanning electron microscopy (FESEM) images were recorded using a Nova NanoSEM450 field emission scanning electron microscope. Transmission electron microscopy (TEM), high-resolution transmission electron microscopy (HRTEM), and selected area electron diffraction (SAED) images were recorded on a FEI TalosF200X field emission transmission electron microscope. The elemental mappings of the samples were determined by the energy-dispersive X-ray spectrometer (EDX) equipped on FESEM and TEM. Nitrogen gas porosimetry measurements were performed on a Quantachrome NOVA 2000e surface area and porosity analyzer after the samples were outgassed under a vacuum at 70 °C for 20 min and 150 °C for 6 h. X-ray diffraction (XRD) patterns were obtained using a D8ADVANCE diffractometer via $\text{Cu-K}\alpha$ radiation with the 2θ angle scanning range of 10–90°. Fourier transform infrared (FTIR) spectra were recorded on a Nicolet iS5 FTIR apparatus. X-ray photoelectron spectra (XPS) was performed using an Axis Ultra DLD instrument with a monochromated $\text{Al-K}\alpha$ source at a residual gas pressure of less than 10^{-8} Pa. All the binding energies were referenced to the C 1 s peak at 284.8 eV of the surface adventitious carbon. UV-visible/diffuse reflectance spectroscopy (UV-vis/DRS) was conducted using a Lambda 750S UV/VIS/NIR spectrometer. Photoluminescence (PL) measurements were carried out on a HITACHI F-7000 fluorescence spectrophotometer under the condition of 400 V operating voltage.

2.4. Photocatalytic tests in the single-component photocatalytic systems and multi-component synergistic photocatalytic systems

A PLS-SXE 300 Xe lamp (300 W, Beijing PerfectLight Co. Ltd., China) with an output wavelength $\lambda > 320$ nm served as the simulated sunlight source. 100 mg of photocatalyst and 100 mL of reaction solution were poured into a 250 mL beaker with a quartz cover. No matter in the single-component photocatalytic systems or multi-component synergistic photocatalytic system, the concentrations of 4-FP, Cr(VI), and As(III) was 20, 10, and 20 mg/L, respectively. The pH of the reaction solution was adjusted with dilute HCl. The suspension was ultrasonicated for 10 min and stirred in dark until adsorption–desorption equilibrium. Subsequently, the light source was switched on, and fixed amounts of the reaction solution were extracted at pre-determined time intervals during irradiation. Changes in the 4-FP concentrations were analyzed using an Agilent 1100 series high-performance liquid chromatography (HPLC): C_{18} column, UV detector ($\lambda = 277$ nm), and acetonitrile/water (60/40 v/v) was used as a mobile phase at a flow rate of 1.0 mL/min. Changes in the Cr(VI) concentrations were analyzed by a diphenylcarbazide method using Lambda 750S UV/VIS/NIR spectrometer at $\lambda = 540$ nm. Changes in the As(V) concentrations were

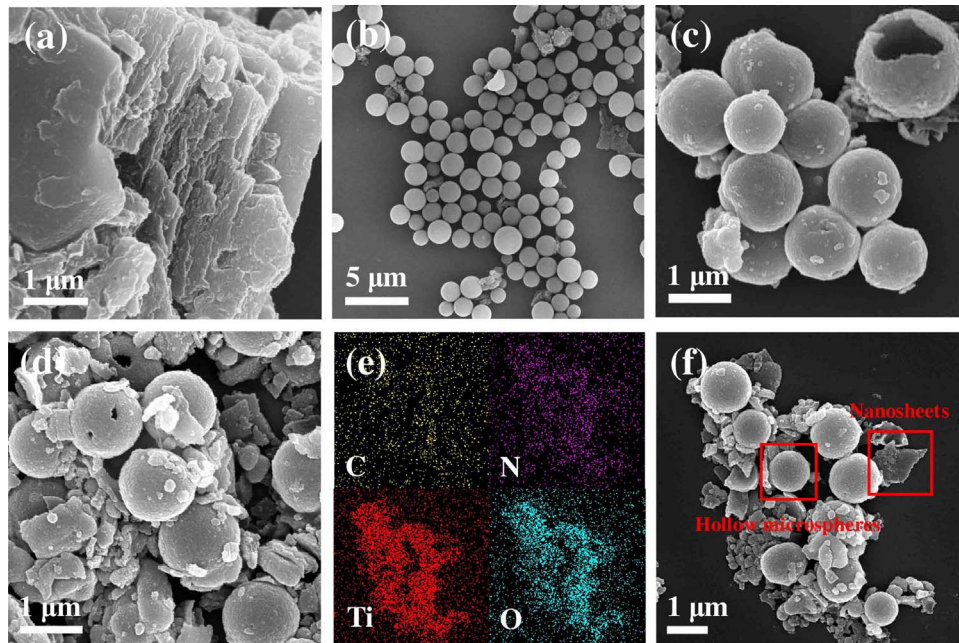


Fig. 1. FESEM images of bulk $\text{g-C}_3\text{N}_4$ (a), HCMSs template (b), TiO_2 HMSs (c), and $\text{g-C}_3\text{N}_4$ NSs/ TiO_2 HMSs (d); EDX elemental mappings (e) of $\text{g-C}_3\text{N}_4$ NSs/ TiO_2 HMSs from selected area (f) for C, N, Ti, and O regions.

analyzed by a molybdenum-blue method using Lambda 750S UV/VIS/NIR spectrometer at $\lambda = 880$ nm, and the concentration of As(III) was calculated by total As minus As(V).

3. Results and discussion

3.1. Characterizations

3.1.1. Morphology and textural property

The morphology of as-prepared materials was preliminarily studied by FESEM observation. As shown in Fig. 1a, bulk $\text{g-C}_3\text{N}_4$ exhibits a graphite-like layered structure with more than five layers. A large number of spherical microstructures observed from Fig. 1b indicate that HCMSs were successfully fabricated by the hydrothermal carbonization of waste *Camellia oleifera* shells according to our previous work [44,45]. Considerable spherical microstructures observed in the TiO_2 HMSs indicate that the self-assembly between HCMSs and TBT is successfully carried out in the preparation process (Fig. 1c). An individual incomplete microsphere indicates that the as-prepared TiO_2 HMSs have hollow spherical microstructures (insert in Fig. 1c). As shown in Fig. 1d, we can clearly observe the coexistence of nanosheets and hollow microspheres in the $\text{g-C}_3\text{N}_4$ NSs/ TiO_2 HMSs. This result indicates that $\text{g-C}_3\text{N}_4$ nanosheets and TiO_2 hollow microspheres are simultaneously constructed by the dispersion and structure-directing effects of HCMSs. The EDX elemental mappings from selected area show that C, N, Ti, and O elements homogeneously distribute throughout the $\text{g-C}_3\text{N}_4$ NSs/ TiO_2 HMSs (Fig. 1e and f). This result indicates that the atomic level hybridization was successfully achieved between the semiconductor components in the $\text{g-C}_3\text{N}_4$ NSs/ TiO_2 HMSs due to the one-step introduction of melamine and TBT precursors.

The morphology of as-prepared materials was further studied by TEM observation. As shown in Fig. 2a, a large number of hollow microspheres with uniform wall thickness were observed in the TiO_2 HMSs. From the TEM image of $\text{g-C}_3\text{N}_4$ NSs/ TiO_2 HMSs we can clearly observe that the $\text{g-C}_3\text{N}_4$ nanosheets and TiO_2 hollow microspheres are combined together in a uniformly dispersed state (Fig. 2b). The simultaneous construction of $\text{g-C}_3\text{N}_4$ nanosheets and TiO_2 hollow microspheres in the $\text{g-C}_3\text{N}_4$ NSs/ TiO_2 HMSs not only facilitates the surface migration of photogenerated carriers in a semiconductor component but also is beneficial to the transfer of photogenerated carriers between the interfaces of two semiconductor components. Compare with TiO_2

HMSs, the lattice spacing of (101) plane in the anatase phase is enlarged for the $\text{g-C}_3\text{N}_4$ NSs/ TiO_2 HMSs, indicating that the lattice doping of C and N elements is achieved in the TiO_2 HMSs component during the $\text{g-C}_3\text{N}_4$ NSs/ TiO_2 HMSs preparation (Fig. 2c and d). The lattice defects formed by lattice doping are favorable for the separation of photogenerated carriers. The SAED patterns of TiO_2 HMSs and $\text{g-C}_3\text{N}_4$ NSs/ TiO_2 HMSs confirm the anatase crystal structure of as-prepared materials, and the rings from the inner to the outer correspond to (101), (004), (200), (105/211), and (204) lattice diffraction in the anatase titanium dioxide (Fig. 2e and i). As shown in Fig. 2f–h, the hollow spherical microstructures can be clearly observed in the EDX elemental mappings of TiO_2 HMSs from selected area, indicating the very high resolution of EDX spectrometer equipped on TEM. For the $\text{g-C}_3\text{N}_4$ NSs/ TiO_2 HMSs, the EDX elemental mappings from selected area indicate that Ti/O or C/N elements are evenly dispersed in an individual $\text{g-C}_3\text{N}_4$ nanosheets or TiO_2 hollow microspheres (Fig. 2j–n). This result further confirms the atomic level hybridization between the semiconductor components in the $\text{g-C}_3\text{N}_4$ NSs/ TiO_2 HMSs. The atomic level hybridization between the semiconductor components further promotes the transfer of photogenerated carriers between the semiconductor components.

The textural property of as-prepared materials was studied by the nitrogen gas adsorption-desorption isotherms and pore-size distribution curves analysis (Fig. 3). As shown in Fig. 3a, bulk $\text{g-C}_3\text{N}_4$ shows a type II isotherm with no hysteresis loop indicating its non-porous bulk layered structure characteristic. The type IV isotherm with H3-type hysteresis loop for the $\text{g-C}_3\text{N}_4$ / TiO_2 indicates that the mesoporous structures are constructed by the accumulation of TiO_2 component. The type IV isotherm with H4-type hysteresis loop for the TiO_2 HMSs can be attributed to the constructed mesoporous structures by the accumulation of hollow microspheres structural units. The type IV isotherm with H4-type hysteresis loop for the $\text{g-C}_3\text{N}_4$ NSs/ TiO_2 HMSs can be attributed to the constructed mesoporous structures by the accumulation of nanosheets and hollow microspheres structural units. As shown in Fig. 3b, we can't observe the BJH (Barrett–Joyner–Halenda) pore-size distribution peak corresponding to the bulk $\text{g-C}_3\text{N}_4$ due to its non-porous bulk layered structure characteristic. The narrow or broad BJH pore-size distribution peak centered at 3.8 or 25.3 nm for the $\text{g-C}_3\text{N}_4$ / TiO_2 can be attributed to the constructed mesoporous structures by the accumulation of TiO_2 nanoparticles or bulk TiO_2 . For the TiO_2 HMSs, the BJH pore-size distribution peak centered at 3.8 or 8.0 nm can be

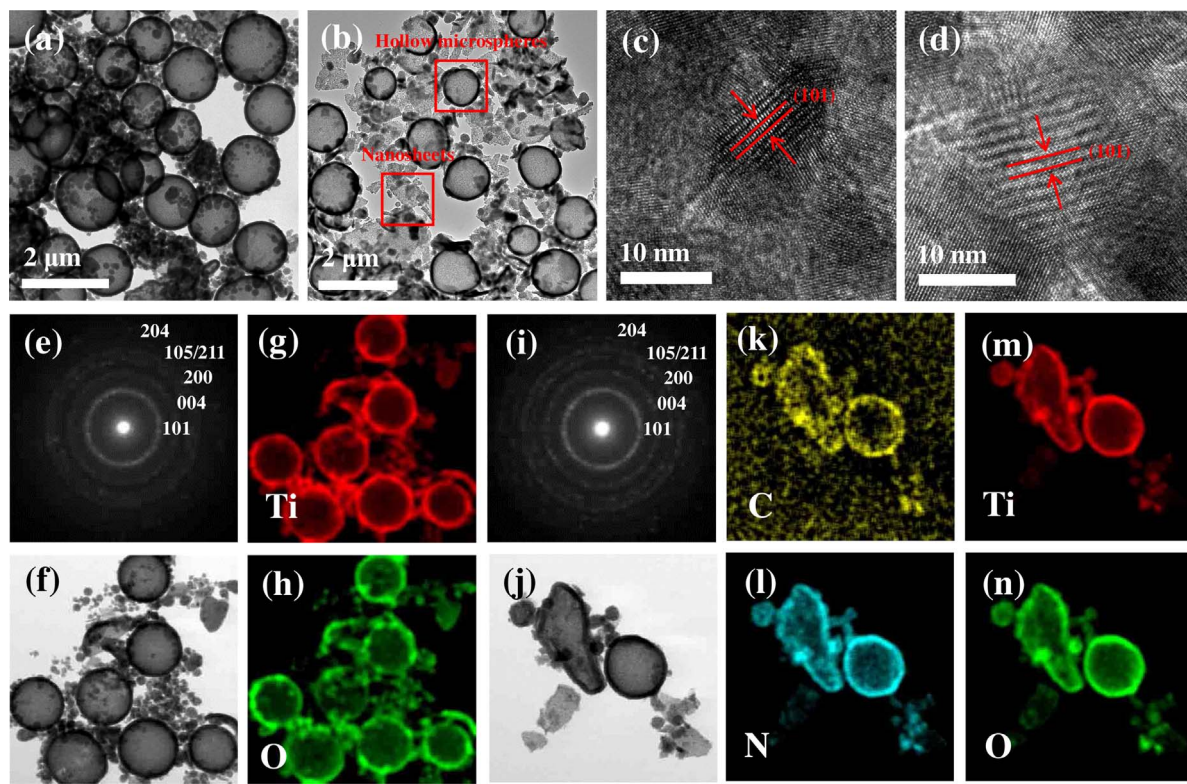


Fig. 2. TEM, HRTEM, and SAED images of TiO_2 HMSs (a, c, and e) and $\text{g-C}_3\text{N}_4$ NSs/ TiO_2 HMSs (b, d, and i); EDX elemental mappings of TiO_2 HMSs (g and h) and $\text{g-C}_3\text{N}_4$ NSs/ TiO_2 HMSs (k, l, m, n) from selected area (f and j).

attributed to the constructed mesoporous structures by the accumulation of TiO_2 nanoparticles or TiO_2 hollow microspheres. For the $\text{g-C}_3\text{N}_4$ NSs/ TiO_2 HMSs, the BJH pore-size distribution peak centered at 3.8, 4.6, or 6.9 nm can be attributed to the constructed mesoporous structures by the accumulation of TiO_2 nanoparticles, $\text{g-C}_3\text{N}_4$ nanosheets, or TiO_2 hollow microspheres. The BET (Brunauer–Emmett–Teller) specific surface areas of bulk $\text{g-C}_3\text{N}_4$ and $\text{g-C}_3\text{N}_4/\text{TiO}_2$ are small due to their bulk structure characteristics prepared in the absence of HCMSSs. The relatively large BET specific surface area for the TiO_2 HMSs can be attributed to the construction of hollow spherical microstructures. For the $\text{g-C}_3\text{N}_4$ NSs/ TiO_2 HMSs, the largest BET specific surface area in the tested samples can be attributed to the simultaneous construction of $\text{g-C}_3\text{N}_4$ nanosheets and TiO_2 hollow microspheres by the dispersion and structure-directing effects of HCMSSs.

3.1.2. Compositional and structural information

The phase structures of as-prepared materials are studied by the wide angle XRD in the range of 10–90° (Fig. 4a). As shown in the XRD pattern of bulk $\text{g-C}_3\text{N}_4$, the strong (002) peak at 27.4° corresponds to its interlayer distance of $d = 0.33$ nm, whereas the (100) peak at 12.8° represents its in-plane structural packing motif with a period of 0.675 nm. The as-prepared TiO_2 HMSs exhibits a pure anatase crystal phase with the characteristic diffractions at 25.3° (101), 38.0° (004), 48.1° (200), 54.1° (105), 55.1° (211), 62.8° (204), 69.0° (116), and 70.3° (220) respectively (JCPDS No. 21–1272). For the $\text{g-C}_3\text{N}_4$ NSs/ TiO_2 HMSs, the simultaneous presence of $\text{g-C}_3\text{N}_4$ and TiO_2 characteristic XRD peaks indicates the coexistence of $\text{g-C}_3\text{N}_4$ and TiO_2 components in the composite. The lattice defects of as-prepared $\text{g-C}_3\text{N}_4$ NSs/ TiO_2 HMSs can be further studied by the narrow angle XRD in the range of 20–30° (Fig. 4b). Compare with bulk $\text{g-C}_3\text{N}_4$, the lower (002) peak intensity of $\text{g-C}_3\text{N}_4$ NSs component in the $\text{g-C}_3\text{N}_4$ NSs/ TiO_2 HMSs indicates that the layered $\text{g-C}_3\text{N}_4$ structural units are reduced in the composite due to the construction of $\text{g-C}_3\text{N}_4$ nanosheets by the dispersion effects of HCMSSs. The (101) peak of TiO_2 HMSs component in the $\text{g-C}_3\text{N}_4$ NSs/ TiO_2 HMSs are broadened and moves to a lower angle

with respect to that of TiO_2 HMSs, indicating that the anatase lattice defects exist due to the introduction of C and N elements in the TiO_2 HMSs component. According to the Bragg equation, the (101) plane lattice spacing of TiO_2 HMSs component in the $\text{g-C}_3\text{N}_4$ NSs/ TiO_2 HMSs is larger than that of TiO_2 HMSs, which is consistent with the HRTEM results shown in Fig. 2c and d. Based on our previous work, the lattice defects can not only prolong the lifetime of photogenerated carriers by capturing the charge carriers but also transfer the captured charge carriers to the reactants [46].

The chemical structures of as-prepared materials are studied by the FTIR spectra shown in Fig. 5. For the TiO_2 HMSs, the broad peak in the 420–1000 cm^{-1} is attributed to the stretching vibration of $\text{Ti}=\text{O}=\text{Ti}$ covalent bonds, and the peaks centered at 1638 and 3409 cm^{-1} are assigned to the $\text{H}=\text{O}=\text{H}$ bending and $\text{O}=\text{H}$ stretching vibration of adsorbed H_2O and surface $-\text{OH}$ groups. For the bulk $\text{g-C}_3\text{N}_4$, the sharp peak at 809 cm^{-1} is the typical bending vibration of s-triazine units, a series of peaks found in the 1000–1600 cm^{-1} can be attributed to the stretching vibration of $\text{C}=\text{N}$ and $\text{C}=\text{N}$ in the CN heterocycles, and the broad peak centered at 3179 cm^{-1} originate from the stretching vibration of primary ($-\text{NH}_2$) and secondary ($=\text{NH}$) amines groups. For the $\text{g-C}_3\text{N}_4$ NSs/ TiO_2 HMSs, the coexistence of $\text{g-C}_3\text{N}_4$ and TiO_2 FTIR characteristic modes indicates the coexistence of $\text{g-C}_3\text{N}_4$ and TiO_2 components in the composite. The FTIR characteristic modes of $\text{g-C}_3\text{N}_4$ NSs component in the $\text{g-C}_3\text{N}_4$ NSs/ TiO_2 HMSs exhibit a higher resolution compare with that of bulk $\text{g-C}_3\text{N}_4$ owing to the more exposed surface functional groups of $\text{g-C}_3\text{N}_4$ NSs component by the construction of $\text{g-C}_3\text{N}_4$ nanosheets. In addition, the disappeared FTIR characteristic mode of surface $\text{Ti}=\text{OH}$ groups in the $\text{g-C}_3\text{N}_4$ NSs/ TiO_2 HMSs indicates that the surface $\text{C}=\text{NH}_2$ groups of $\text{g-C}_3\text{N}_4$ NSs react with the surface $\text{Ti}=\text{OH}$ groups of TiO_2 HMSs to form $\text{C}=\text{NH}=\text{Ti}$ covalent bonds between the interfaces of $\text{g-C}_3\text{N}_4$ NSs and TiO_2 HMSs components.

The interactions between elements or components in the $\text{g-C}_3\text{N}_4$ NSs/ TiO_2 HMSs can be studied by high-resolution XPS in the C 1s, N 1s, Ti 2p, and O 1s binding energy regions. For the C 1s XPS of bulk $\text{g-C}_3\text{N}_4$, the peak centered at 284.8 eV is typically assigned to $\text{C}=\text{C}$ or/and

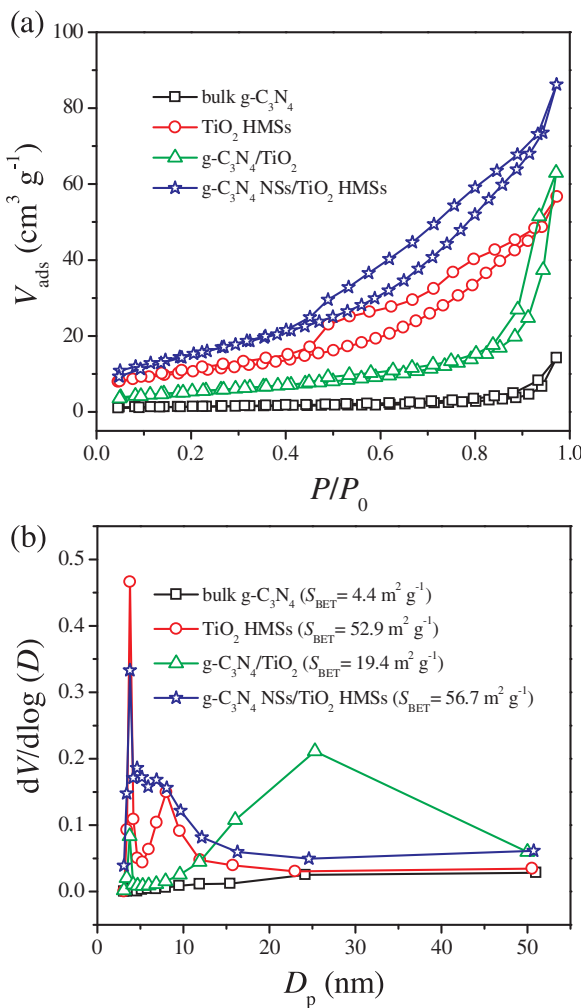


Fig. 3. Nitrogen gas adsorption-desorption isotherms (a) and pore-size distribution curves (b) of as-prepared materials.

$\text{C}=\text{C}$, which originates from the adventitious reference carbon on the tested materials surface; the peak centered at 288.2 eV originates from sp^2 C atoms bonded to N in an aromatic ring ($\text{N}=\text{C}-(\text{N})_2$), whereas the peak centered at 289.1 eV is assigned to sp^2 C atoms in the aromatic ring attached to the primary ($\text{N}=\text{C}(\text{N})-\text{NH}_2$) or secondary ($\text{N}=\text{C}(\text{N})-\text{NH}$) amine (Fig. 6a). For the N 1 s XPS of bulk $\text{g-C}_3\text{N}_4$, the peak centered at 398.7 eV is assigned to sp^2 -hybridized aromatic nitrogen atoms bonded to carbon atoms ($\text{C}=\text{N}-\text{C}$), the peak centered at 400.4 eV is related to either tertiary nitrogen groups ($(\text{C})_3-\text{N}$) linking structural motifs (C_6N_7) or amino groups carrying hydrogen ($(\text{C})_2-\text{NH}$, $\text{C}-\text{NH}_2$) in connection with structural defects and incomplete condensation, the peak at 401.2 eV corresponds to nitrogen atoms bonded to three carbon atoms in the aromatic cycles ($\text{N}-(\text{C})_3$), and a weak peak at 404.5 eV is attributed to charging effects or positive charge localization in heterocycles (Fig. 6b). For the Ti 2p XPS of TiO_2 HMSs, the determined binding energies of $\text{Ti 2p}_{3/2}$ and $\text{Ti 2p}_{1/2}$ are 458.5 and 464.3 eV, which are in good agreement with anatase TiO_2 (Fig. 6c). For the O 1 s XPS of TiO_2 HMSs, two peaks with the binding energies of 529.8 and 531.7 eV can be attributed to the lattice-oxygen ($\text{Ti}-\text{O}$) and hydroxyl-oxygen ($\text{O}-\text{H}$) in anatase TiO_2 . The C 1s, N 1s, Ti 2p, and O 1s XPS peaks of $\text{g-C}_3\text{N}_4$ NSs/TiO₂ HMSs slightly shift to a higher binding energy direction with respect to bulk $\text{g-C}_3\text{N}_4$ and TiO_2 HMSs. This result further confirms the correctness of the above conclusion. On the one hand, the atomic level hybridization was successfully achieved between the semiconductor components in the $\text{g-C}_3\text{N}_4$ NSs/TiO₂ HMSs due to the one-step introduction of melamine and TBT precursors. On the other hand,

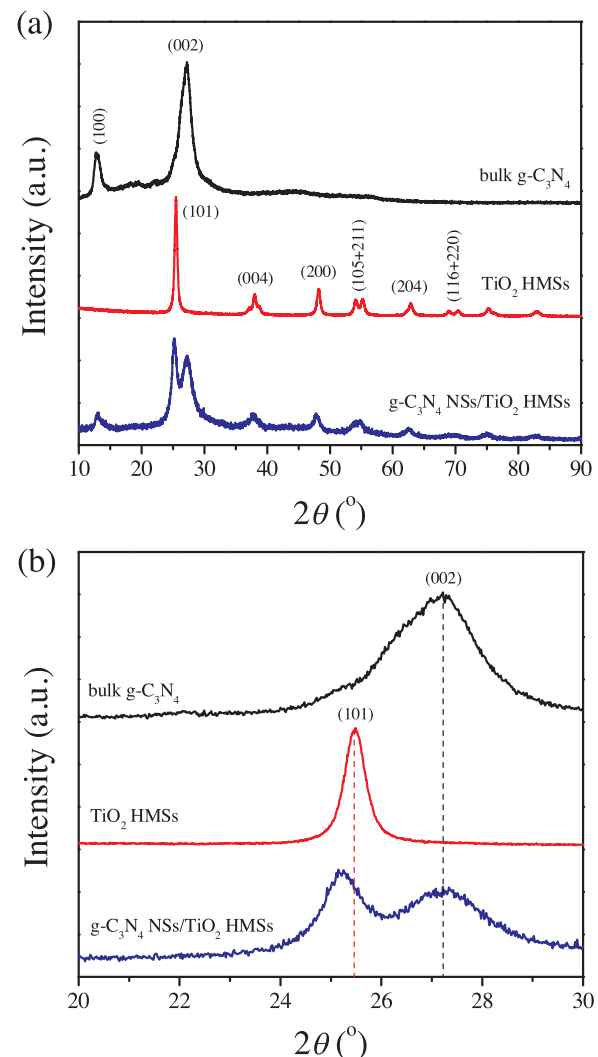


Fig. 4. XRD patterns of as-prepared materials in the range of 10–90° (a) and 20–30° (b).

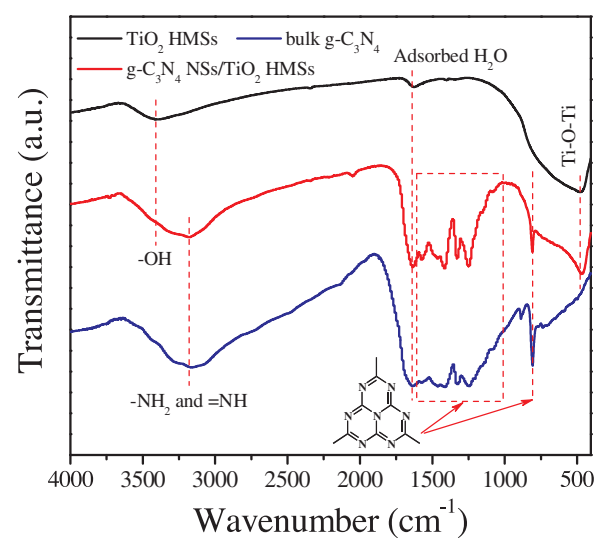


Fig. 5. FTIR spectra of as-prepared materials.

the surface $\text{C}-\text{NH}_2$ groups of $\text{g-C}_3\text{N}_4$ NSs react with the surface $\text{Ti}-\text{OH}$ groups of TiO_2 HMSs to form a $\text{C}-\text{NH}-\text{Ti}$ covalent bond between the interfaces of $\text{g-C}_3\text{N}_4$ NSs and TiO_2 HMSs components.

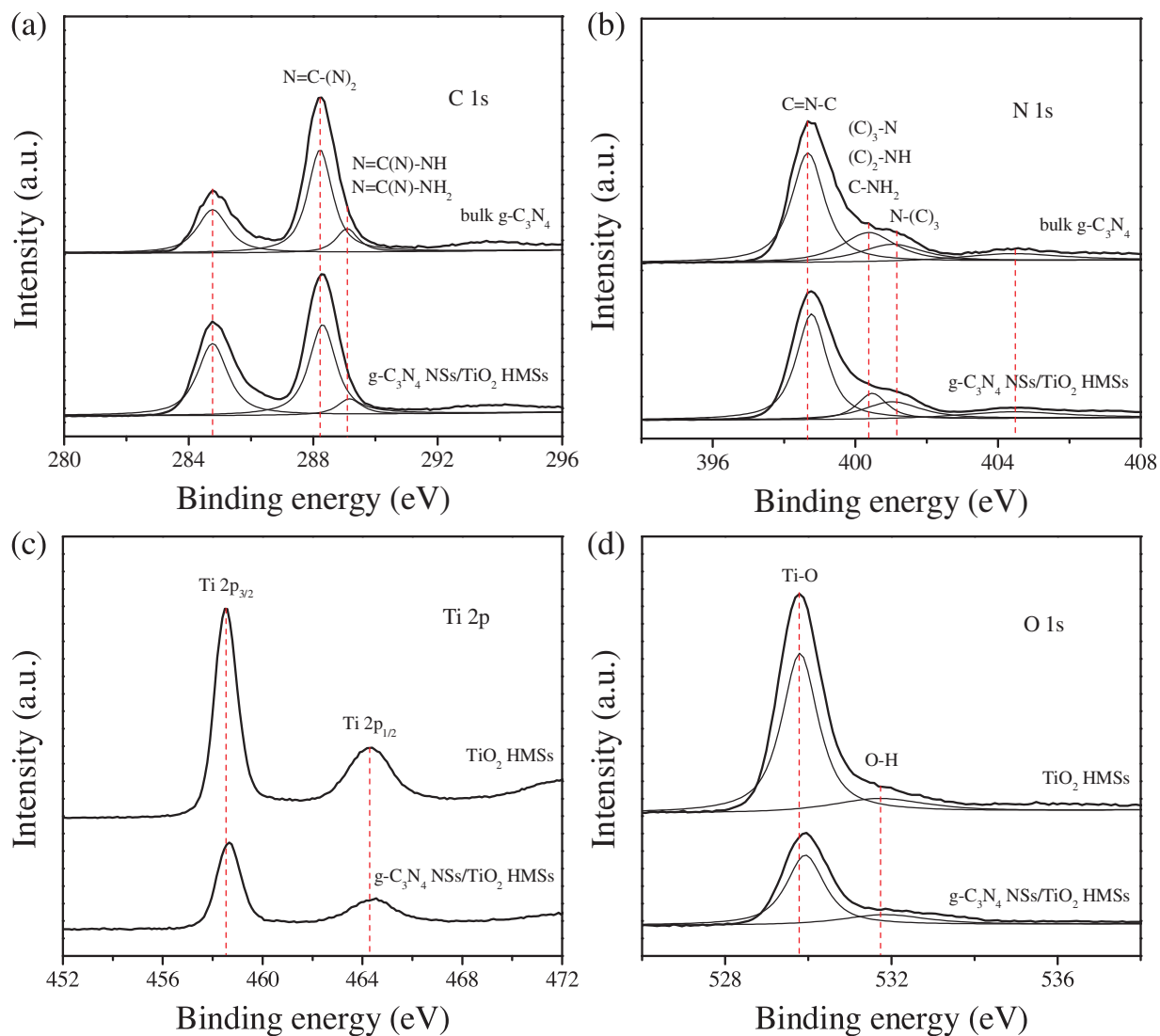


Fig. 6. High-resolution XPS of as-prepared materials in the C 1s (a), N 1s (b), Ti 2p (c), and O 1s (d) binding energy regions.

3.1.3. Optical and electronic properties

The light absorption properties of as-prepared materials are studied by UV-vis/DRS. As shown in Fig. 7, bulk $\text{g-C}_3\text{N}_4$ shows a typical semiconductor light absorption in the 200–450 nm, which originates

from the electronic transition from the valence band (VB) populated by N 2p orbit to the conduction band (CB) formed by C 2p orbit. For the TiO_2 HMSs, a strong light absorption in the 200–400 nm can be attributed to the electronic transition from VB (O 2p) to CB (Ti 3d). In the UV-vis/DRS of $\text{g-C}_3\text{N}_4$ NSs/ TiO_2 HMSs, a complete semiconductor light absorption signal was observed, and the light absorption signals corresponding to the $\text{g-C}_3\text{N}_4$ NSs and TiO_2 HMSs components can't be observed. This result also indicates that the atomic level hybridization was successfully achieved between the semiconductor components in the $\text{g-C}_3\text{N}_4$ NSs/ TiO_2 HMSs due to the one-step introduction of melamine and TBT precursors. In addition, the light absorption signal exists in the 430–800 nm for the $\text{g-C}_3\text{N}_4$ NSs/ TiO_2 HMSs can be attributed to the small amount of residual carbon that comes from ethanol solvent and HCMSS template, because the released NH_3 from the polycondensation of melamine inhibits the removal of carbon component.

The photocatalytic quantum efficiencies of as-prepared materials were studied by PL measurements. All the materials were tested under the condition of 400 V operating voltage. For comparison, bulk $\text{g-C}_3\text{N}_4$ was physically mixed with barium sulfate according to the mass ratio of $\text{g-C}_3\text{N}_4$ in the $\text{g-C}_3\text{N}_4/\text{TiO}_2$ before testing. As shown in Fig. 8, bulk $\text{g-C}_3\text{N}_4$ exhibits a strong fluorescence emission peak in the 400–600 nm, suggesting that a large number of photoinduced $e^- - h^+$ pairs are generated and rapidly recombined within the bulk $\text{g-C}_3\text{N}_4$. The fluorescence emission peak of TiO_2 HMSs can't be observed in Fig. 8,

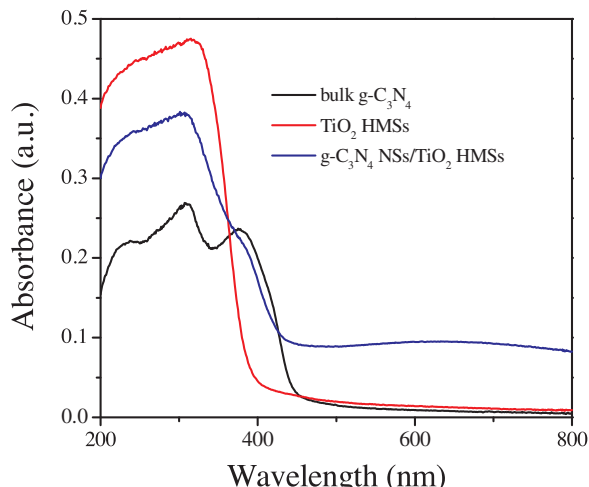


Fig. 7. UV-vis/DRS of as-prepared materials.

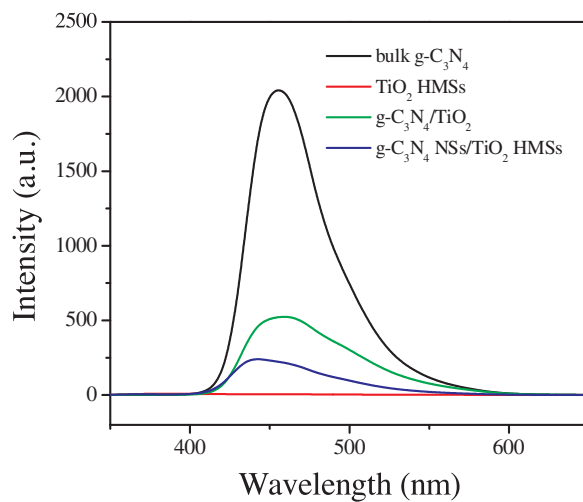


Fig. 8. PL spectra of as-prepared materials.

indicating that TiO_2 HMSs can't be excited under the condition of 400 V operating voltage. Compare with bulk $\text{g-C}_3\text{N}_4$, the obviously decreased intensity of fluorescence emission peak for the $\text{g-C}_3\text{N}_4/\text{TiO}_2$ can be attributed to the efficient transportation of photogenerated carriers between the semiconductor components. Compare with $\text{g-C}_3\text{N}_4/\text{TiO}_2$, the further decreased intensity of fluorescence emission peak for the $\text{g-C}_3\text{N}_4$

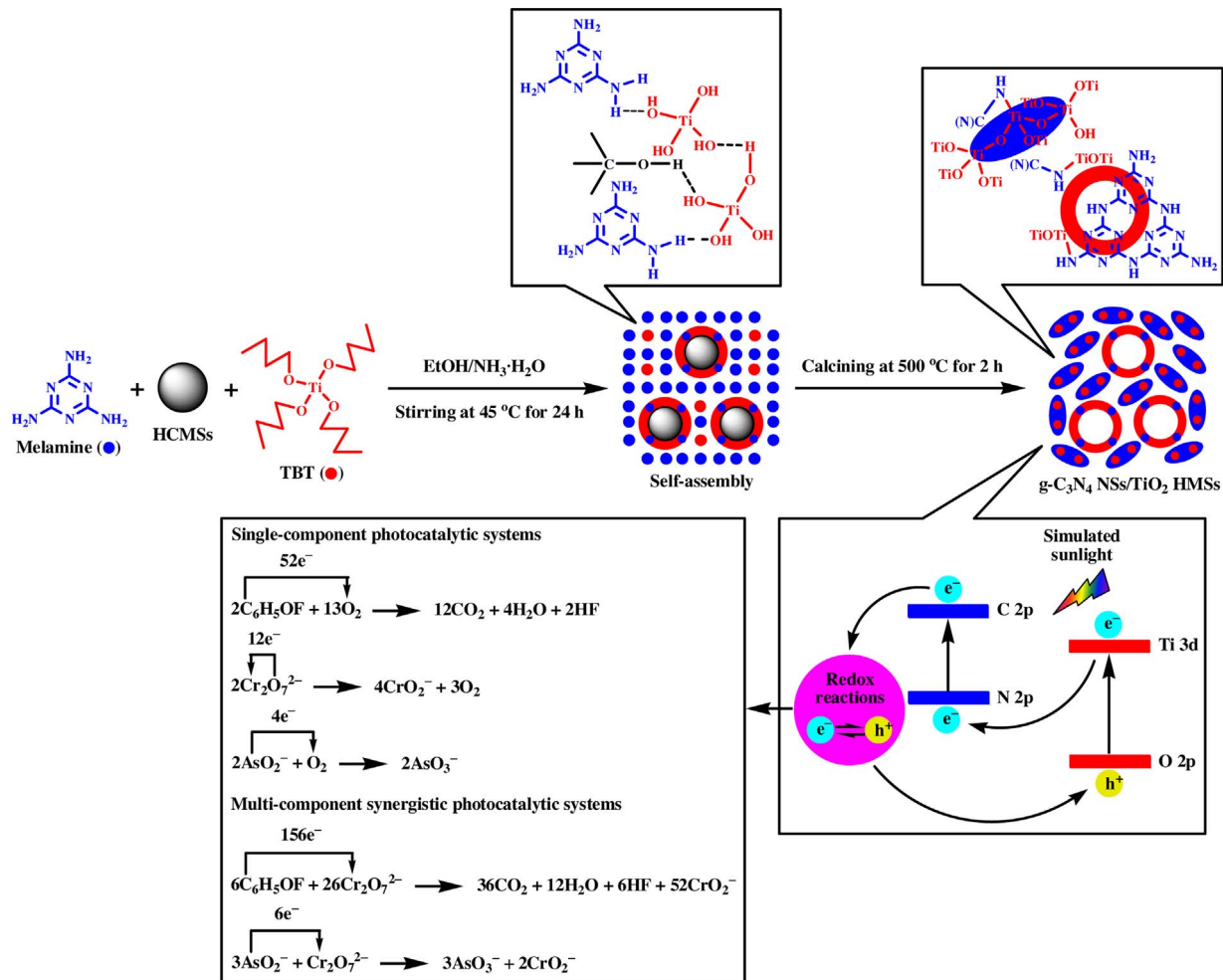
NSs/ TiO_2 HMSs indicates that the more efficient separation and transportation of photogenerated carriers are realized after the simultaneous construction of $\text{g-C}_3\text{N}_4$ nanosheets and TiO_2 hollow microspheres.

Based on the above discussion of the characterization results, the proposed route for one-step fabrication of $\text{g-C}_3\text{N}_4$ NSs/ TiO_2 HMSs with atomic level hybridization and the separation and transportation of photoinduced charge carriers in the $\text{g-C}_3\text{N}_4$ NSs/ TiO_2 HMSs under simulated sunlight irradiation are shown in **Scheme 1**. When stirring the HCMSSs/melamine/TBT/EtOH/ $\text{NH}_3\text{H}_2\text{O}$ suspension at 45 °C, the self-assembly among HCMSSs, melamine, and TBT precursors was achieved by hydrogen bonding. After calcining at 500 °C for 2 h, the HCMSSs template was removed and the polycondensation of the precursors (melamine and TBT) was completed. Finally, $\text{g-C}_3\text{N}_4$ NSs/ TiO_2 HMSs with atomic level hybridization was successfully fabricated.

3.2. Photocatalytic tests

3.2.1. 4-FP degradation, Cr(VI) reduction, and As(III) oxidation single-component photocatalytic systems

The photocatalytic tests were conducted in an aqueous solution containing oxygen from dissolved air. The photocatalytic activities of as-prepared materials were preliminarily evaluated in the 4-FP degradation, Cr(VI) reduction, and As(III) oxidation single-component photocatalytic systems. The adsorption results shown in **Fig. 9a–c** indicate that the adsorption–desorption equilibrium has been achieved between target contaminants and photocatalysts before the simulated



Scheme 1. The proposed route for one-step fabrication of $\text{g-C}_3\text{N}_4$ NSs/ TiO_2 HMSs with atomic level hybridization and the synergistic photocatalytic mechanisms in the multi-component composite pollution systems.

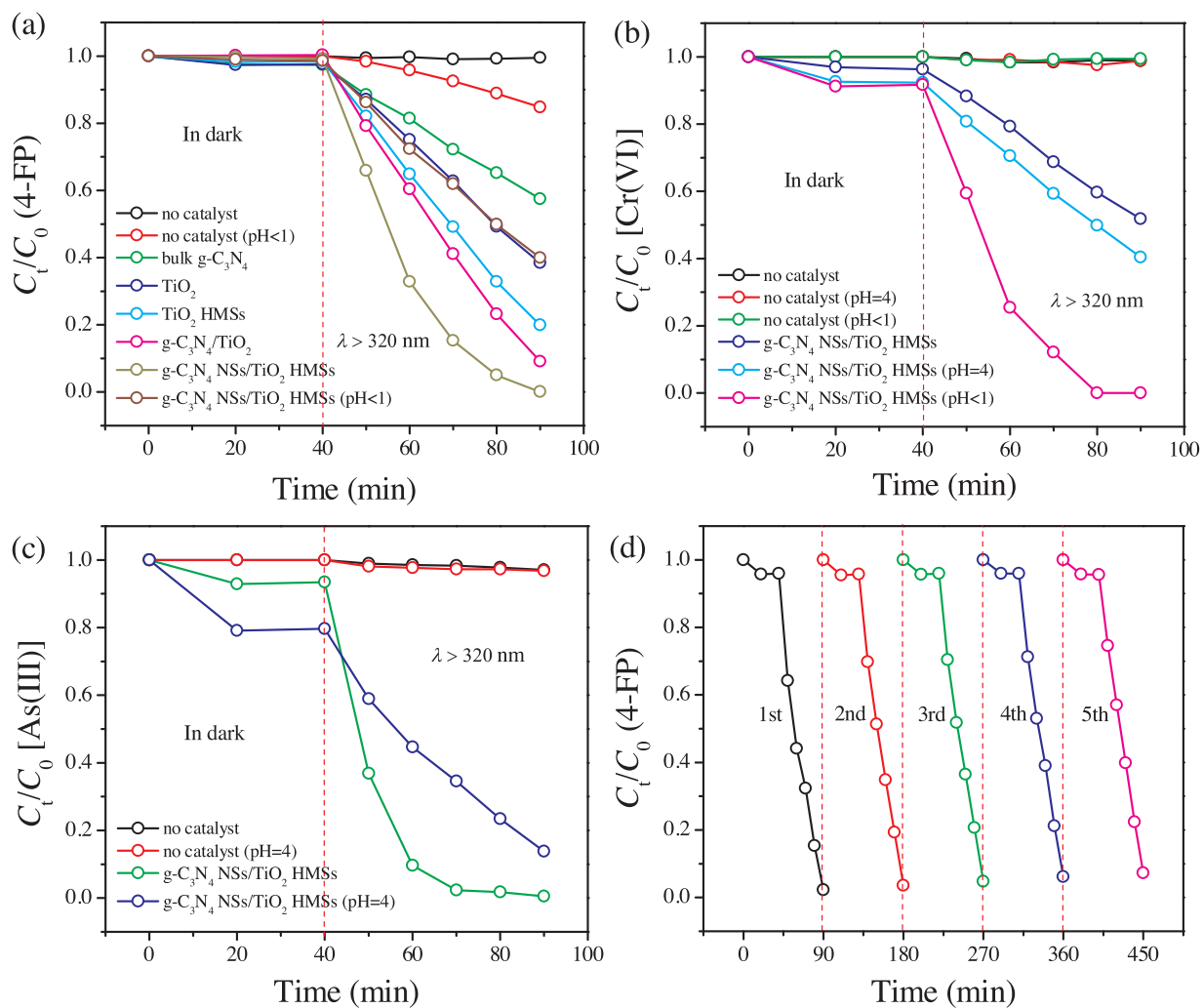


Fig. 9. Adsorption and photocatalytic degradation of 4-FP (a), reduction of Cr(VI) (b), and oxidation of As(III) (c) by using as-prepared materials under simulated sunlight irradiation; recycling experiments of photocatalytic degradation of aqueous 4-FP over g-C₃N₄ NSs/TiO₂ HMSs photocatalyst (d). M (catalyst) = 100 mg, V (reaction solution) = 100 mL, C_0 (4-FP) = 20 mg/L, C_0 [Cr(VI)] = 10 mg/L, C_0 [As(III)] = 20 mg/L.

sunlight irradiation. For the 4-FP degradation system shown in Fig. 9a, the direct photodegradation experiments (on catalyst) show that the change of 4-FP concentration is negligible under neutral condition but the 4-FP concentration decrease somewhat after the simulated sunlight irradiation for 50 min under acidic condition. The above result is due to the fact that H^+ causes the decrease of 4-FP electron cloud density, resulting in the decrease of 4-FP stability. The photocatalytic activities of as-prepared materials for the 4-FP degradation followed the order of bulk g-C₃N₄ < TiO₂ ≈ g-C₃N₄ NSs/TiO₂ HMSs (pH < 1) < TiO₂ HMSs < g-C₃N₄/TiO₂ < g-C₃N₄ NSs/TiO₂ HMSs. The photocatalytic activity of TiO₂ is higher than that of bulk g-C₃N₄ due to the higher photocatalytic quantum efficiency of TiO₂. Compare with TiO₂, the increased photocatalytic activities of TiO₂ HMSs and g-C₃N₄/TiO₂ can be attributed to the construction of hollow spherical microstructure and semiconductor heterojunctions. The obviously increased photocatalytic activity of g-C₃N₄ NSs/TiO₂ HMSs compared with that of g-C₃N₄/TiO₂ can be attributed to the simultaneous construction of g-C₃N₄ nanosheets and TiO₂ hollow microspheres in the g-C₃N₄ NSs/TiO₂ HMSs. The photocatalytic activity of g-C₃N₄ NSs/TiO₂ HMSs is obviously decreased under acidic condition because the quenching of photogenerated electrons caused by H^+ is detrimental to the formation of hydroxyl radicals ($\cdot OH$). For the Cr(VI) reduction system shown in Fig. 9b, the blank tests (on catalyst) show that aqueous Cr(VI) can't be reduced under both acidic and neutral conditions due to the lack of photogenerated electrons. The reduction rate of Cr(VI) is gradually accelerated with

gradually reducing the pH value of photocatalytic system, because the electron cloud density of oxygen in the $Cr_2O_7^{2-}$ is reduced by H^+ , resulting in facilitating the reduction of Cr(VI) by photogenerated electrons. For the As(III) oxidation system shown in Fig. 9c, the blank tests (on catalyst) show that the change of As(III) concentrations is negligible under both acidic and neutral conditions due to the lack of $\cdot OH$. The oxidation rate of As(III) is obviously decreased under acidic condition also because the quenching of photogenerated electrons caused by H^+ is disadvantageous for the formation of $\cdot OH$.

The above 4-FP degradation reaction was repeated for five times to evaluate the stability of as-prepared g-C₃N₄ NSs/TiO₂ HMSs. After the first catalytic run, the catalyst was recovered by centrifugation. The recovered catalyst was used for the subsequent catalytic runs under the same experimental conditions. As shown in Fig. 9d, the as-prepared g-C₃N₄ NSs/TiO₂ HMSs exhibits considerably high stability in the current 4-FP degradation photocatalytic system, and it can maintain a similar level of reactivity after five catalytic cycles. A slightly decreased photocatalytic activity can be attributed to the loss of photocatalyst in the recovery process.

3.2.2. 4-FP/Cr(VI) and Cr(VI)/As(III) multi-component synergistic photocatalytic systems

In the 4-FP/Cr(VI) and Cr(VI)/As(III) multi-component synergistic photocatalytic systems, the degradation of 4-FP, reduction of Cr(VI), and oxidation of As(III) can be simultaneously carried out under both

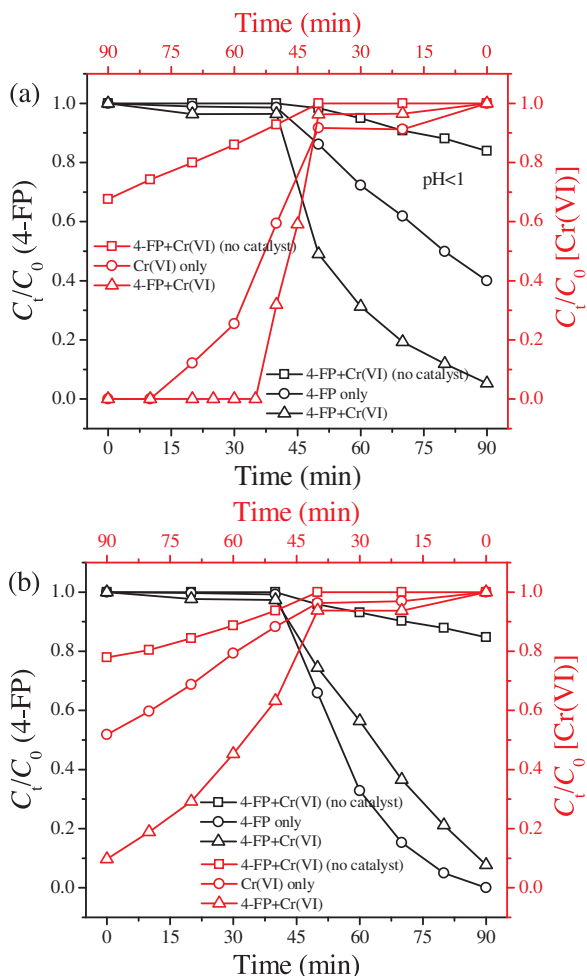


Fig. 10. Simultaneous photocatalytic reduction of Cr(VI) with 4-FP degradation by using as-prepared $\text{g-C}_3\text{N}_4$ NSs/ TiO_2 HMSs photocatalyst under acidic (a) and neutral (b) conditions. M (catalyst) = 100 mg, V (reaction solution) = 100 mL, C_0 (4-FP) = 20 mg/L, C_0 [Cr(VI)] = 10 mg/L.

acidic and neutral conditions and a synergistic photocatalytic effect exists in the above multi-component composite pollution systems. As shown in Fig. 10 and 11, the adsorption results indicate that the adsorption–desorption equilibrium has been achieved between target contaminants and photocatalysts before the simulated sunlight irradiation. The blank tests (on catalyst) show that the concentrations of 4-FP, Cr(VI), and As(III) were hardly decreased under both acidic and neutral conditions, indicating that the redox reaction between 4-FP and Cr(VI) or between Cr(VI) and As(III) is difficult to carry out in dilute solution. The concentration of contaminants in the 4-FP/Cr(VI) or Cr(VI)/As(III) multi-component synergistic photocatalytic system is twice that of the 4-FP degradation, Cr(VI) reduction, or As(III) oxidation single-component photocatalytic system. However, the total photocatalytic reaction efficiency is obviously improved owing to the existence of synergistic photocatalytic effects in the 4-FP/Cr(VI) or Cr(VI)/As(III) multi-component composite pollution system.

As shown in Fig. 10a, compare with 4-FP degradation and Cr(VI) reduction single-component photocatalytic systems, both the degradation efficiency of 4-FP and the reduction efficiency of Cr(VI) were simultaneously improved in the 4-FP/Cr(VI) multi-component synergistic photocatalytic system under $\text{pH} < 1$ acidic condition. This result implies that a new photocatalytic reaction has been carried out in addition to the individual photocatalytic degradation of 4-FP or reduction of Cr(VI), thus generating a synergistic photocatalytic effect in the 4-FP/Cr(VI) multi-component synergistic

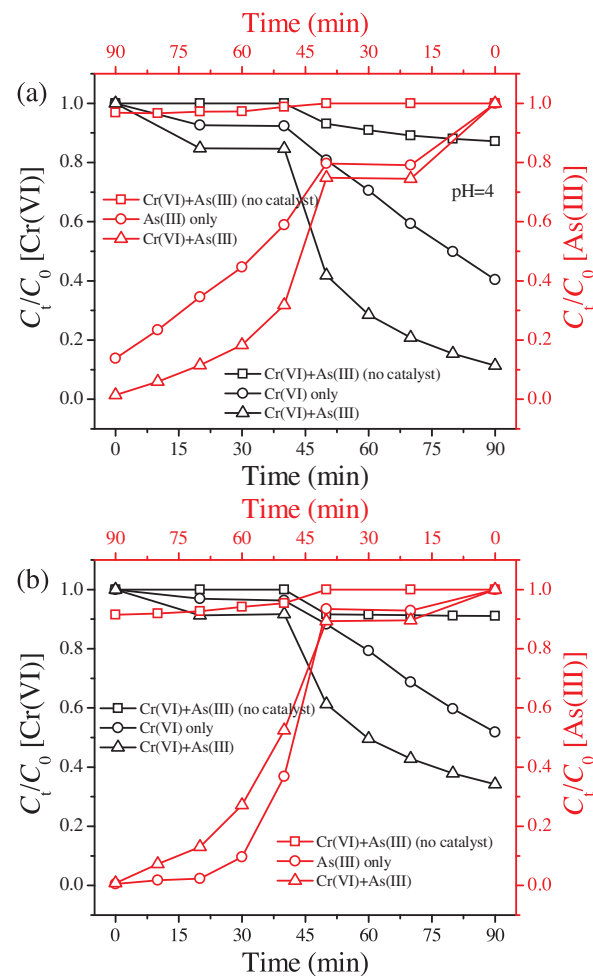


Fig. 11. Simultaneous photocatalytic reduction of Cr(VI) with As(III) oxidation by using as-prepared $\text{g-C}_3\text{N}_4$ NSs/ TiO_2 HMSs photocatalyst under acidic (a) and neutral (b) conditions. M (catalyst) = 100 mg, V (reaction solution) = 100 mL, C_0 [Cr(VI)] = 10 mg/L, C_0 [As(III)] = 20 mg/L.

photocatalytic system under $\text{pH} < 1$ acidic condition. In the 4-FP/Cr(VI) multi-component synergistic photocatalytic system without adjusting pH (neutral condition), the degradation efficiency of 4-FP was slightly declined and the reduction efficiency of Cr(VI) was significantly improved compared with 4-FP degradation and Cr(VI) reduction single-component photocatalytic systems (Fig. 10b). This result further demonstrates that a synergistic photocatalytic effect exists in the 4-FP/Cr(VI) multi-component synergistic photocatalytic system under neutral condition.

The photocatalytic tests results in the Cr(VI)/As(III) multi-component synergistic photocatalytic system are similar to the above photocatalytic tests results in the 4-FP/Cr(VI) multi-component synergistic photocatalytic system. As shown in Fig. 11a, both the reduction efficiency of Cr(VI) and the oxidation efficiency of As(III) were simultaneously improved in the Cr(VI)/As(III) multi-component synergistic photocatalytic system compared with Cr(VI) reduction and As(III) oxidation single-component photocatalytic systems under $\text{pH} = 4$ acidic condition. As shown in Fig. 11b, the reduction efficiency of Cr(VI) was significantly improved and the oxidation efficiency of As(III) was slightly declined compared with Cr(VI) reduction and As(III) oxidation single-component photocatalytic systems under neutral condition (without adjusting pH). The above results indicate that the synergistic photocatalytic effects also exist in the Cr(VI)/As(III) multi-component synergistic photocatalytic system under both acidic and neutral conditions.

3.2.3. Discussion of reaction mechanisms in the multi-component synergistic photocatalytic systems

In our previous studies, we have cleared that all the photocatalytic reactions belong to the redox processes and photocatalysts act as electron transfer mediums in the redox processes if the intermediate steps of the photocatalytic reactions are neglected [47,48]. Specifically, dissolved O_2 acts as an oxidizing agent and 4-FP acts as a reducing agent in the 4-FP degradation single-component photocatalytic system, Cr(VI) acts as an oxidizing agent and O^{2-} in the $Cr_2O_7^{2-}$ acts as a reducing agent in the Cr(VI) reduction single-component photocatalytic system, and dissolved O_2 acts as an oxidizing agent and As(III) acts as a reducing agent in the As(III) oxidation single-component photocatalytic system (Scheme 1). In addition to the above redox reactions in the single-component photocatalytic systems, the redox reaction between 4-FP and Cr(VI) or between Cr(VI) and As(III) was switched on by the electron transfer of the photocatalyst in the 4-FP/Cr(VI) or Cr(VI)/As(III) multi-component synergistic photocatalytic system (Scheme 1). Therefore, compare with 4-FP degradation, Cr(VI) reduction, and As(III) oxidation single-component photocatalytic systems, the total photocatalytic reaction efficiencies are improved in the 4-FP/Cr(VI) and Cr(VI)/As(III) multi-component synergistic photocatalytic systems (Fig. 10 and 11). That is, the synergistic photocatalytic effects exist in the 4-FP/Cr(VI) and Cr(VI)/As(III) multi-component composite pollution systems. In the 4-FP/Cr(VI) or Cr(VI)/As(III) multi-component composite pollution system with adjusting pH < 1 or pH = 4 by dilute HCl, the redox reaction between 4-FP and Cr(VI) or between Cr(VI) and As(III) was easily carried out by the electron transfer of the photocatalyst in the presence of H^+ because of the low electron cloud density of oxygen in the $Cr_2O_7^{2-}$. Therefore, an obvious synergistic photocatalytic effect was shown in the 4-FP/Cr(VI) or Cr(VI)/As(III) multi-component composite pollution system with adjusting pH < 1 or pH = 4 by dilute HCl (Figs. 10a and 11a). However, in the 4-FP/Cr(VI) or Cr(VI)/As(III) multi-component composite pollution system without adjusting pH, the electron cloud density of oxygen in the $Cr_2O_7^{2-}$ is high. Therefore, the redox reaction between 4-FP and Cr(VI) or between Cr(VI) and As(III) was inhibited in the 4-FP/Cr(VI) or Cr(VI)/As(III) multi-component composite pollution system without adjusting pH (Figs. 10b and 11b). In addition, compare with 4-FP degradation and As(III) oxidation single-component photocatalytic systems, the slightly lower degradation efficiency of 4-FP and oxidation efficiency of As(III) in the 4-FP/Cr(VI) or Cr(VI)/As(III) multi-component composite pollution system without adjusting pH can be attributed to the competitive effects of pollutant components on the photogenerated electrons.

4. Conclusions

The $g\text{-}C_3N_4$ NSs/TiO₂ HMs with excellent photocatalytic activity was successfully fabricated by a simple one-step synthesis strategy in the assistance of HCMs. HCMs act as both dispersant and structure-directing agent for the simultaneous construction of $g\text{-}C_3N_4$ nanosheets and TiO₂ hollow microspheres. The atomic level hybridization was successfully achieved between the semiconductor components in the $g\text{-}C_3N_4$ NSs/TiO₂ HMs due to the one-step introduction of melamine and TBT precursors. The excellent photocatalytic activity of $g\text{-}C_3N_4$ NSs/TiO₂ HMs can be attributed to the simultaneous construction of $g\text{-}C_3N_4$ nanosheets and TiO₂ hollow microspheres and the atomic level hybridization of semiconductor components in the $g\text{-}C_3N_4$ NSs/TiO₂ HMs. The synergistic photocatalytic effects existed in the 4-FP/Cr(VI) or Cr(VI)/As(III) multi-component composite pollution system due to the fact that the redox reaction between 4-FP and Cr(VI) or between Cr(VI) and As(III) was switched on by the electron transfer of the photocatalyst.

Acknowledgements

This work was financially supported by the Major International (Regional) Joint Research Program of China (51720105001); the National Natural Science Foundation of China (51568049, 21366024, 51238002, 51272099, 21665018, 51468043); the National Science Fund for Excellent Young Scholars (51422807); the Natural Science Foundation of Jiangxi Province, China (20161BAB206118, 20171ACB21035); Distinguished Youth Science Fund of Jiangxi Province, China (20162BCB23043); the Natural Science Foundation of Jiangxi Provincial Department of Education, China (GJJ14515).

References

- M. Muz, M. Krauss, S. Kutsarova, T. Schulze, W. Brack, Environ. Sci. Technol. 51 (2017) 1830–1839.
- Z. Chen, X. Li, J. Wang, L. Tao, M. Long, S.J. Liang, L.K. Ang, C. Shu, H.K. Tsang, J.B. Xu, ACS Nano 11 (2017) 430–437.
- X. Wang, N. Maeda, A. Baiker, ACS Catal. 6 (2016) 7898–7906.
- Z. Li, X. Xu, W. Zhang, X. Meng, W. Ma, A. Yartsev, O. Inganäs, M.R. Andersson, R.A.J. Janssen, E. Wang, J. Am. Chem. Soc. 138 (2016) 10935–10944.
- R. Tong, C. Liu, Z. Xu, Q. Kuang, Z. Xie, L. Zheng, ACS Appl. Mater. Interfaces 8 (2016) 21326–21333.
- H. Liu, H. Zhang, P. Shen, F. Chen, S. Zhang, Langmuir 32 (2016) 254–264.
- K. Ullah, S. Ye, Z. Lei, K.Y. Cho, W.C. Oh, Catal. Sci. Technol. 5 (2015) 184–198.
- S.F. Hung, Y.C. Yu, N.T. Suen, G.Q. Tzeng, C.W. Tung, Y.Y. Hsu, C.S. Hsu, C.K. Chang, T.S. Chan, H.S. Sheu, J.F. Lee, H.M. Chen, Chem. Commun. 52 (2016) 1567–1570.
- T. Zhang, Y. Shen, Y. Qiu, Y. Liu, R. Xiong, J. Shi, J. Wei, ACS Sustainable Chem. Eng. 5 (2017) 4630–4636.
- C.Y. Tsai, C.W. Liu, C. Fan, H.C. His, T.Y. Chang, J. Phys. Chem. C 121 (2017) 6050–6059.
- X. Yue, S. Yi, R. Wang, Z. Zhang, S. Qiu, J. Mater. Chem. A 5 (2017) 10591–10598.
- M. Xiong, L. Chen, Q. Yuan, J. He, S.L. Luo, C.T. Au, S.F. Yin, Carbon 86 (2015) 217–224.
- M. Xiong, L. Chen, Q. Yuan, J. He, S.L. Luo, C.T. Au, S.F. Yin, Dalton Trans. 43 (2014) 8331–8337.
- J. Xue, S. Ma, Y. Zhou, Z. Zhang, M. He, ACS Appl. Mater. Interfaces 7 (2015) 9630–9637.
- D. Lu, H. Wang, X. Zhao, K.K. Kondamareddy, J. Ding, C. Li, P. Fang, ACS Sustainable Chem. Eng. 5 (2017) 1436–1445.
- M. Sun, T. Yan, Q. Yan, H. Liu, L. Yan, Y. Zhang, B. Du, RSC Adv. 4 (2014) 19980–19986.
- S. Weon, W. Choi, Environ. Sci. Technol. 50 (2016) 2556–2563.
- M. Misra, N. Singh, R.K. Gupta, Catal. Sci. Technol. 7 (2017) 570–580.
- Y. Choi, M.S. Koo, A.D. Bokare, D. Kim, D.W. Bahnemann, W. Choi, Environ. Sci. Technol. 51 (2017) 3973–3981.
- W. Wang, J. Fang, S. Shao, M. Lai, C. Lu, Appl. Catal. B Environ. 217 (2017) 57–64.
- X. Shi, M. Fujitsuka, Z. Lou, P. Zhang, T. Majima, J. Mater. Chem. A 5 (2017) 9671–9681.
- J. Liu, B. Cheng, J. Yu, Phys. Chem. Chem. Phys. 18 (2016) 31175–31183.
- W. Zhou, W. Li, J.Q. Wang, Y. Qu, Y. Yang, Y. Xie, K. Zhang, L. Wang, H. Fu, D. Zhao, J. Am. Chem. Soc. 136 (2014) 9280–9283.
- M.K. Hossain, A.R. Koirala, U.S. Akhtar, M.K. Song, K.B. Yoon, Chem. Mater. 27 (2015) 6550–6557.
- T. Wang, X. Meng, G. Liu, K. Chang, P. Li, Q. Kang, L. Liu, M. Li, S. Ouyang, J. Ye, J. Mater. Chem. A 3 (2015) 9491–9501.
- S. Yang, Y. Gong, J. Zhang, L. Zhan, L. Ma, Z. Fang, R. Vajtai, X. Wang, P.M. Ajayan, Adv. Mater. 25 (2013) 2452–2456.
- S. Liu, S.B. Mishra, Y. Zhang, L. Qi, ACS Sustainable Chem. Eng. 5 (2017) 1509–1516.
- M. Palomo, A. Peñalver, C. Aguilar, F. Borrull, J. Hazard. Mater. 181 (2010) 716–721.
- J. Krajčovičová, A.Q. Eschenroeder, Environ. Sci. Technol. 41 (2007) 6847–6853.
- A. Fujishima, K. Honda, Nature 238 (1972) 37–38.
- Y. Gui, Q. Ma, X. Deng, Q. Meng, X. Cheng, M. Xie, X. Li, Q. Cheng, H. Liu, Appl. Catal. B Environ. 206 (2017) 136–145.
- F. Chen, Q. Yang, Y. Wang, J. Zhao, D. Wang, X. Li, Z. Guo, H. Wang, Y. Deng, C. Niu, G. Zeng, Appl. Catal. B: Environ. 205 (2017) 133–147.
- Y. Liu, Q. Wu, Y. Zhao, Dalton Trans. 46 (2017) 6425–6432.
- F. Chen, Q. Yang, J. Sun, F. Yao, S. Wang, Y. Wang, X. Wang, X. Li, C. Niu, D. Wang, G. Zeng, ACS Appl. Mater. Interfaces 8 (2016) 32887–32900.
- S.F. Yang, C.G. Niu, D.W. Huang, H. Zhang, C. Liang, G.M. Zeng, Environ. Sci. Nano 4 (2017) 585–595.
- H. Yoneyama, Y. Yamashita, H. Tamura, Nature 282 (1979) 817–818.
- J. Ding, J. Ming, D. Lu, W. Wu, M. Liu, X. Zhao, C. Li, M. Yang, P. Fang, Catal. Sci. Technol. 7 (2017) 2283–2297.
- S.H. Yoon, S.E. Oh, J.E. Yang, J.H. Lee, M. Lee, S. Yu, D. Pak, Environ. Sci. Technol. 43 (2009) 864–869.
- W. Choi, J. Yeo, J. Ryu, T. Tachikawa, Tetsuro Majima, Environ. Sci. Technol. 44 (2010) 9099–9104.

- [40] M. Rakibuddin, S. Mandal, R. Ananthakrishnan, *New J. Chem.* 41 (2017) 1380–1389.
- [41] N.C. Birben, M.C. Paganini, P. Calza, M. Bekbolet, *Photochem. Photobiol. Sci.* 16 (2017) 24–30.
- [42] Y. Zhang, J. Shi, Y. Hu, Z. Huang, L. Guo, *Catal. Sci. Technol.* 6 (2016) 8080–8088.
- [43] S. Liu, G. Huang, J. Yu, T.W. Ng, H.Y. Yip, P.K. Wong, *ACS Appl. Mater. Interfaces* 6 (2014) 2407–2414.
- [44] K. Zhao, S. Liu, K. Li, Z. Hu, Y. Yuan, L. Yan, H. Guo, X. Luo, *Mol. Catal.* 433 (2017) 193–201.
- [45] W. Ma, K. Li, H. Guo, L. Yan, Y. Dai, X. Luo, Y. Yao, *Micropor. Mesopor. Mater.* 250 (2017) 195–202.
- [46] K. Li, X. Yang, Y. Guo, F. Ma, H. Li, L. Chen, Y. Guo, *Appl. Catal. B: Environ.* 99 (2010) 364–375.
- [47] K. Li, Z. Zeng, L. Yan, M. Huo, Y. Guo, S. Luo, X. Luo, *Appl. Catal. B Environ.* 187 (2016) 269–280.
- [48] K. Li, Z. Zeng, L. Yan, S. Luo, X. Luo, M. Huo, Y. Guo, *Appl. Catal. B Environ.* 165 (2015) 428–437.